# Dynamic Control of Nanopore Wetting in Water and Saline Solutions under an Electric Field

Davide Vanzo, Dusan Bratko,* and Alenka Luzar*

Department of Chemistry, Virginia Commonwealth University, Richmond, Virginia 23284-2006, United States

ABSTRACT: Field-induced nanopore wetting by aqueous solutions, including electrolytes, provides opportunities for a variety of applications. Conflicting porosity requirements have so far precluded direct implementations of a two-way control: the pores have to be sufficiently wide to allow water infiltration at experimentally relevant voltages but should not exceed the kinetic threshold for spontaneous expulsion in the absence of the field. Applicable widths are restricted below a few nanometers. Only a narrow window of fields and pore geometries can *simultaneously* satisfy both of the above requirements. Accurate accounts of wetting equilibria *and* dynamics at nanoscale porosity require molecular level descriptions. Here we use molecular dynamics simulations to study dynamic, field-controlled transitions between nanoconfined liquid and vapor phases in contact with an unperturbed aqueous or electrolyte environment. In nanopores wetted by electrolyte solutions, we observe depletion of salt compared to the bulk phase. The application of a local electric field enhances the uptake of water and ions in the confinement. In systems prone to capillary evaporation, the process can be reversed at sufficient strength of the electric field. For alternating displacement field, we identify the conditions where O (ns) responses of the reversible infiltration/expulsion cycle can be secured for experimentally realizable field strengths, porosity, and salinity of the solution.
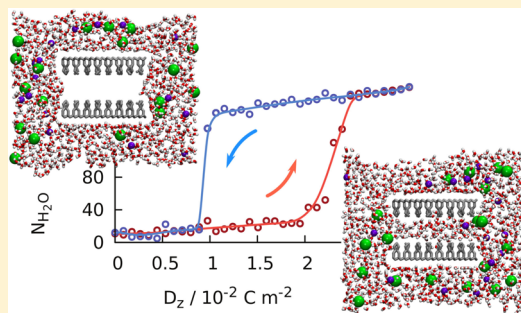
I. INTRODUCTION

Transient wetting of hydrophobic nanochannels or pores is of interest for a range of applications including hydrophobic valves,[1,2] control of membrane permeability,[3] energy storage in porous substrates,[4−8] and regulated wettability.[9] Affinity between the pore and water can be modulated by a variety of external stimuli, including light,[2] temperature,[10] pH,[2] pressure,[8,11,12] or electric field.[1,2,12−22] Because of the comparative ease of application, and fast and uniform control, several experimental studies[1,2] examined the use of applied field in *dynamic* wetting experiments. Together with related studies concerned with capillary condensation,[19,23,24] these works show wetting of hydrophobic nanopores could generally be induced by the field. However, at *above* a few nm porosity, reversible dewetting of pores surrounded by an aqueous bath presents a challenge, with the wetted state kinetically stalled[2] because of high activation barriers for evaporation.[25−33]

Descending to narrow $O(1)$ nm pores, in this work, we demonstrate the possibility of *complete*, fully reversible filling/ emptying cycles by using molecular dynamics (MD) simulations. Molecular approach is essential, as aqueous nanoconfinements show important quantitative and qualitative deviations from the continuum picture,[34,35] both in the absence[26,28,30,36−41] and presence[13,16−18,21,22,42−44] of an applied electric field. Main differences can be explained in terms of interfacial hydrogen bonding,[45−48] responsible for anisotropic polarizability of aqueous interfaces and associated field-direction effects.[18,21,44,48,49] In short, the lateral component of the permittivity tensor in a nanoscale slit is about twice bigger than the normal one. Likewise, the field-induced increase

in surface wettability is notably stronger in a parallel than normal field. When the field is applied across the pore, a Janus interface can emerge, with the wetting propensity at the wall under the incoming field exceeding the one in the outgoing field.[18,44,48] Anisotropy in polarization *dynamics* of interfacial water revealed in recent MD simulations[50] can be even more pronounced than for static properties. These effects are negligible at the macroscopic level but can modulate the phase behavior in nanoscale systems, characterized by strong representation of surface molecules.

Below, we describe the first simulation study of dynamic, field-controlled wetting/drying transitions in nanoconfined aqueous solutions. Because of the potential role dissolved ions *could* play in these electrostatically driven processes,[14,51,52] we consider both the neat water and electrolyte solutions. As described in the Model and Methods section, our approach builds on the methodology we developed in a recent study of equilibrated, fully wetted pores under a static electric field.[22] The pore is immersed in an unperturbed bath at constant peripheral pressure and fixed chemical potential. We describe a generalization to uniformly varying fields across the confinement. We monitor the system evolution upon abruptly or gradually changing the displacement field in the nanopore to induce water infiltration or expulsion. To suppress the barrier

to spontaneous expulsion, we use very narrow pores, which in turn require stronger electric fields to trigger infiltration. Continuum electrostatics offers rough estimates of the threshold electric displacement field, D_z, while we deduce the profile of the electric field E_z, modulated by dielectric screening, from the simulation results. Insights into filling/expulsion equilibria in confinements *surrounded by liquid bath*, obtained in our study, are readily applicable to the reverse problem of capillary condensation from and evaporation to the surrounding vapor phase.[19,23,24] A separate study would, however, be needed to characterize the distinct transition kinetics in the latter scenario.

In the Results section, we compare temporal profiles of the liquid density inside the nanopores for different increasing or decreasing field rates. For O(nm) wide apolar pores, complete wetting−dewetting cycles can be repeated with no restrictions. We observe only small variations of the infiltration (forward) branches in individual cycles. An insignificant influence of the rate of the field increase implies small or negligible barriers to liquid *infiltration*. The reverse branch, on the other hand, is poorly reproducible. A pronounced hysteresis and large variance of expulsion times are indicative of a notable barrier to expulsion. In view of a rapid increase of the barrier with interwall separation,[25,27,29−33] spontaneous expulsion only takes place at pore widths below a few nm. In salt solutions, narrow widths are conducive to salt depletion.[53] Our simulations show ions entering into, and withdrawing from, the pore together with surrounding water; however, the salt molality is generally lowered inside the confinement. In the uncharged nanosized pores we consider, the presence of salt does not alter the occurrence, or rate, of the observed wetting/drying transitions in any significant way. This observation is indicative of a comparatively weak role of electro-osmotic flow[14] effects. For specified pore and field parameters, it hence supports generalizations of model predictions for nanopore gating to include pure water as well as ionic solutions.

II. MODEL AND METHODS

A. Simulated System. To capture transport processes between the field-exposed confined phase and unperturbed solution, a small model pore is embedded in a bigger field-free reservoir (Figure 1). The temperature is held at 300 K using a Nosé−Hoover thermostat.[54] Constant pressure in the bath, close to the vapor pressure of water, is maintained by pressure buffering,[22,55,56] provided by coexisting liquid and vapor domains. For this purpose, two 7-10 Å wide vapor pockets are created in the regions adjacent to purely repulsive walls, placed at the top and bottom boundaries of the rectangular simulation box, as illustrated in Figure 1. The resulting system is self-barostating in *NVT* ensemble, with vanishing normal component of reservoir pressure. The lateral pressure components are negative consistent with the positive interfacial free energy at the vapor−liquid interface. Water molecules interact with the repulsive walls through a harmonic potential with a spring constant of 84 kJ mol Å^{-2}. A detailed description of the method is given in the preceding work.[22] The box accommodates 8282 water molecules, along with $N_{NaCl} = 153$ ion pairs when modeling 1.027 mol kg^{-1} salt solution.

For easier comparisons with previous studies,[12,13,16−18,22,43,44,57−60] we represent water molecules using the extended simple point charge model (SPC/E).[61] The model has repeatedly been shown to provide satisfactory descriptions of dielectric and interfacial properties[62−67] of
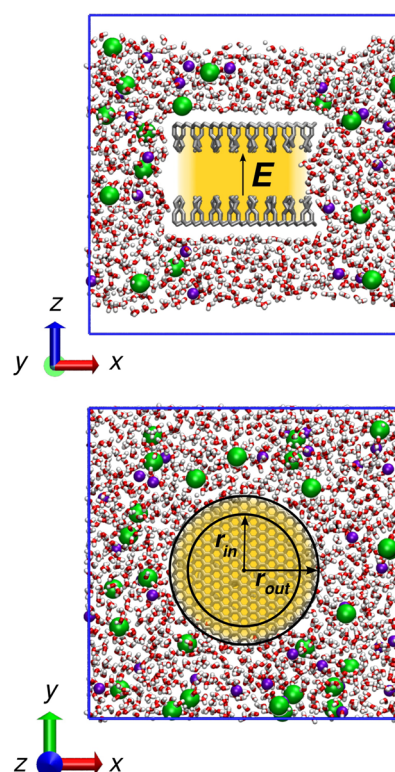
Figure 1. Simulation setup consisting of a rectangular box filled by electrolyte solution. Top: side view of the system, showing the empty hydrophobic confinement between a pair of disk-like platelets made of butylated graphane.[69] The aqueous phase pervading the simulation box is flanked by vapor pockets adjacent to purely repulsive walls at the bottom and top boundaries of the box. Yellow color denotes the region subject to a weak electric field. When the field intensifies, the region is filled by the solution. Bottom: top view of the box showing the regions of uniform ($r < r_{in}$) and fading electric field ($r_{in} < r < r_{out}$). Thin slices of the system are shown for better visualization.

liquid water, an essential requirement for our study. In analogy to other classical-simulation models of water, the SPC/E model does not capture water dissociation. In simulated systems of size of up to 10^4 water molecules, this ignores the rare presence of dissociated ion pairs: at neutral pH, a single pair of ions would on average be present in the simulated system over about 0.01% of the time of observation. While strong electric fields can enhance dissociation of water in microchannels,[68] our calculations at Na$^+$ and Cl$^−$ concentrations as high as 1 mol kg^{-1} reveal at most a minute influence of dissolved ions on the occurrence *and* rate of field-controlled nanopore infiltration and expulsion, the central phenomena of the present study.

In the center of the box, we place a nanopore comprised of a pair of parallel platelets of circular shape. This geometry minimizes the area of the liquid−vapor interface formed in the case of liquid expulsion from the pore, and enables a symmetric decay of the electric field applied across the confinement. To enable spontaneous expulsion of water in the absence of the field, the nanopore walls are made of strongly hydrophobic materials, devoid of polar or ionizing groups. This way, the confinement can switch from strongly hydrophobic in the absence of the applied field to hydrophilic in its presence. Our model pore walls are carved from a plate of butyl-function-alized[69] graphane,[70,71] a hydrogenated form of graphene with a high band gap,[72] and a planar structure insensitive to chemical substitutions. The insulating properties of graphane make it a

suitable prototypical material for simulations in the presence of ions[73] or an externally applied field. In a previous work, we determined the contact angle of water on pure graphane at ~73°.[69] Functionalization by butyl groups with a surface density of 4.01 nm^{-2}, a typical density of physisorbed SAMs layers, brings the contact angle to that of a hydrocarbon.[69,74] To improve computational efficiency, in this work, graphane is modeled using the united-atom representation with hydrocarbon groups described as Lennard-Jones entities with interaction parameters we collect in Table 1. These parameters

Table 1. Lennard-Jones Parameters and Charges Used for the Simulation of Butyl Functionalized Graphane Surfaces and Sodium Chloride Ions[a]

atom	σ (Å)	ε (kcal mol^{-1})	q (e_o)
C, RCH$_3$ (123°)	3.905	0.175	0.00
C, RCH$_3$ (128°)	3.905	0.100	0.00
C, R$_2$CH$_2$	3.905	0.118	0.00
C, R$_3$CH	3.850	0.080	0.00
C, R$_4$C	3.800	0.050	0.00
Na$^+$	2.583	0.100	1.00
Cl$^-$	4.40	0.100	−1.00

[a]Hydrocarbon groups are described by the OPLS-UA (united atom) force field,[93] and the values for ions are taken from Fyta and Netz.[75]

are based on OPLS-UA force fields with the energy constant ε of the terminal −CH$_3$ group parametrized to capture the target contact angle of a strongly hydrophobic hydrocarbon brush. We use Na$^+$ and Cl$^-$ force fields of Fyta and Netz.[75] The ion force fields were parametrized with a Lennard-Jones cutoff of 9 Å; hence, we adopted this cutoff for all Lennard-Jones interactions. Lorentz−Berthelot mixing rules are used to describe water−ion, water−surface, and ion−surface interactions.

The pore wall diameters were 34 or 64 Å, with interplate separation measured between graphane plates at 23 or 31 Å, respectively. Corresponding separations between terminal methyl groups at opposing plates were ~11 or 19 Å. The thickness d of the confined aqueous slab accommodated inside the pore at these separations (measured from the positions of the Gibbs dividing surfaces) was 7 or 15 Å (see Figure 2). The bath water layers above and beneath the confinement spanned around 2−2.5 nm, a thickness proven sufficient to avoid evaporation events within these layers.

Long-range interactions were treated by a particle−particle−particle mesh solver (PPPM) with a real space cutoff of 9 Å and relative precision tolerance in force per atom of 10^{-5}. The Yeh−Berkowitz correction to the Ewald summation[76] was used to account for the two-dimensional periodicity of the system.

B. Contact Angle Measurement. Reversible infiltration and expulsion of water or solution from nanopores requires a careful selection of system properties. Within a continuum approximation, the widths supporting spontaneous liquid expulsion from a cylindrical pore of diameter 2R can be estimated by a modified Kelvin equation for planar confinements of finite lateral size[26]

$$d \leq \frac{2\Delta\gamma}{P + 2\gamma R^{-1}} \tag{1}$$

Here, d is the thickness of the water slab in the pore, P is the external pressure, γ is the surface tension of the liquid, and $\Delta\gamma = -\gamma \cos\theta_c$ is the wetting free energy of the pore walls. Information about the wall contact angle θ_c is therefore
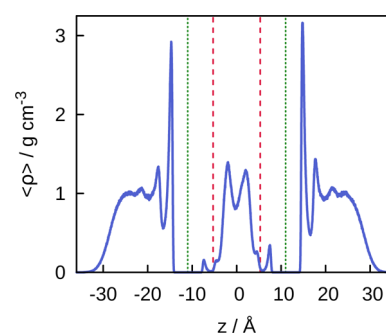

Figure 2. Density profiles of water (blue line) inside the central portion of the simulated system. Vertical lines denote the positions of graphane backbones (dotted green) and terminal methyl groups of butyl functionalizing chains (dashed red lines). The difference in peak heights at the inner and outer confinement surfaces reflects different contact angles, ~128° on the inner (butylated) and 73° on the outer (bare graphane) side. The profiles reveal minute penetration of water into the butyl brush. The asymmetry of the peaks is associated with electric field and polarization of water inside the pore (D_z = 0.031 C m^{-2}). The confinement spontaneously evacuates upon cessation of the field.

important for the design of the system. We determined the contact angle of water on our functionalized surface from the simulations of *cylindrical* nanodroplets as described in a former work.[69] A 6600 molecule nanodrop was placed on a rectangular graphane sheet of dimensions 12.4 × 19.1 nm^2 and the contact angle sampled over several nanoseconds following ~0.1 ns equilibration. The cylindrical drop geometry essentially eliminated line tension effects, providing a good approximation to contact angles converged with respect to the droplet's size. For model parameters from Table 1, with ε_{CH_3} = 0.1 kcal mol^{-1} and a short-range interaction cutoff of 9 Å, the contact angle was 128 ± 3°. To explore the possibility of the contact angle reduction due to the presence of water surrounding the pore, we repeated contact angle calculations on graphane substrate sitting on an ~1.6 nm thick aqueous slab. A statistically insignificant average reduction by 1−2° was found in the presence of the slab.[79] The lack of "wetting transparency",[77,78] observed in contact angle measurements on graphene, is explained by the notably greater thickness of the butylated graphane used in our system.

For nanoscale pore *diameters R* and ambient pressure P, the denominator in eq 1 is dominated by the surface tension term, which reflects the cost of forming the liquid−vapor interface at the pore perimeter. The inequality $\gamma R^{-1} \gg P$ leads to a simpler thermodynamic condition for evaporation, $d < -R \cos\theta_c$. For our smaller pore size, $R \sim 17$ Å, this suggests d should be held below ~11 Å, corresponding to the distance between terminal methyl groups on distinct walls $h \sim 15$ Å (separation between graphane plates ~27 Å). We choose h at 11 Å and $d \sim 7$ Å. As d measures the width available to the centers of water oxygens, the pore accommodates about three layers of water molecules. To observe spontaneous expulsion in wider pores will generally require increasing the lateral dimension of the pore, R. However, while increased R eases the thermodynamic condition for evaporation given by eq 1, liquid can still remain stalled in the pore kinetically. A kinetic barrier to evaporation is known to rapidly increase with the width of the pore. In hydrocarbon nanopores, the barrier becomes prohibitive beyond a few nm width, with metastable liquid persisting
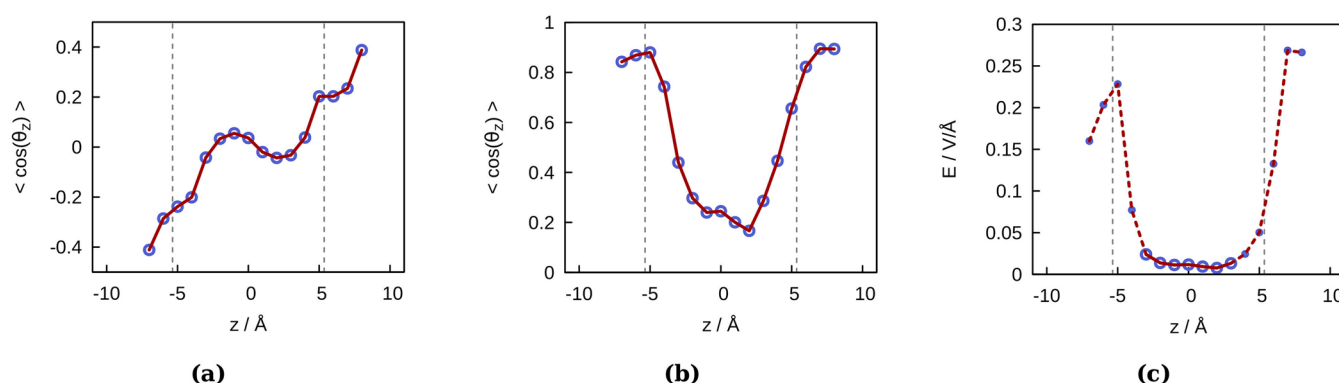
Figure 3. Polarization of water, measured in terms of the average angle between water dipoles and wall normal (z axis) inside 11 Å aqueous confinement: (a) spontaneous polarization in the absence of electric field; (b) displacement field $D_z = 0.031$ C m^{-2}; (c) electric field profile inside the confined aqueous slab. Dashed vertical lines denote the average positions of terminal methyl groups.

over all practically relevant times[25,29−33] even for macroscopic lateral size R.

C. Electric Field. To mimic the conditions between extended hydrophobic walls under a homogeneous field, a uniform electric displacement field $D_z(r) = D_z(0)$, perpendicular to pore walls, is imposed across the core of the cylindrical confinement at distances from the central axis $r < r_{in}$ (Figure 1). The field $\mathbf{D}(r)$ describes the contribution of (implicit) external charges[22] to the local electrostatic potential, $\psi(r, z)$. ε_o is the permittivity of a vacuum, and D_z can be viewed as the surface density of the charge stored in a capacitor. The force acting on a molecular or ion charge q_i due to the imposed field is therefore $\mathbf{F}_i = q_i\mathbf{D}(r)/4\pi\varepsilon_o$. To avoid the complications associated with the MD integration in a discontinuous field,[22] at distances exceeding r_{in}, the field D_z gradually decays over a finite interval $r_{in} \leq r \leq r_{out}$, vanishing at the confinement border, $r = r_{out}$. The field decay with r is described by the relation

$$D_z(r) = D_z(0)g(r) \tag{2}$$

with

$$g(r) = \begin{cases} 1 & \text{for } r_s \leq 0 \\ \frac{1}{2}[\cos(\pi r_s) + 1] & \text{if } 0 \leq r_s \leq 1, \; r_s = \dfrac{r - r_{in}}{r_{out} - r_{in}} \\ 0 & \text{for } r_s > 1 \end{cases}$$

The radial electric displacement field component, $D_r(r, z)$, vanishes in homogeneous regions ($r < r_{in}$ or $r > r_{out}$) but is nonzero within the region of varying $D_z(r)$, $r_{in} \leq r \leq r_{out}$. Since $\mathbf{D}(r, z)$ is a conservative vector field,

$$\frac{\partial^2\psi(r, z)}{\partial z\partial r} = \frac{\partial^2\psi(r, z)}{\partial r\partial z}, \; \text{i.e.,} \; \frac{\partial D_r(r, z)}{\partial z} = \frac{\partial D_z(r, z)}{\partial r} \tag{3}$$

For the specific form of $D_z(r)$, eq 2, and the symmetry condition $D_r(r, 0) = 0$, integration of eq 3 gives

$$D_r(r, z) = zD_z(0)\frac{\partial g(r)}{\partial r} \tag{4}$$

The details of the method, and its advantages over the use of explicit wall charges, are described in ref 22. The smooth variation of the field supports the use of standard MD. Our computations were performed using the LAMMPS simulation package with the velocity Verlet integrator and a simulation time step of 1 fs. The stability of the integrator and the pressure-buffering method were verified in test *NVE* simulations as described in the previous work.[22]

To drive the liquid into a hydrophobic pore, Maxwell stress[14,19,80,81] has to overcome the Laplace pressure associated with unfavorable wetting free energy of the pore. For a pore with finite diameter ($2R$) under a uniform electric displacement field $\mathbf{D} = (0, 0, D_z)$, a first order continuum estimate for the thermodynamic condition for infiltration, analogous to eq 1, takes the form[21,82]

$$d \geq \frac{2\Delta\gamma}{P + \frac{D_z^2}{2\varepsilon_o}\left(1 - \frac{1}{\varepsilon_r}\right) + \frac{2\gamma}{R}} \tag{5}$$

where ε_r approximates the relative permittivity of confined liquid inside a wetted pore. We underscore that the mean-field estimates (eqs 5−7), relying on continuum concepts, serve merely as a ballpark assessment of field effects. More rigorous continuum level analyses of static properties *and* transition dynamics are possible following refs 14 and 52 but are outside the scope of our molecular level study. For $O(nm)$ pore diameters, ambient pressure P can be neglected in comparison to the surface tension term in the denominator. For fixed separation d and $\varepsilon_r^{-1} \ll 1$, eq 5 can be rewritten as a condition for minimal displacement field capable of triggering infiltration into the pore

$$D_z \geq \sqrt{-4\gamma\varepsilon_o(\cos\theta_c \, d^{-1} + R^{-1})} \tag{6}$$

For present pore dimensions, $R = 17$ Å, $d = 7$ Å, and $\gamma_{SPC/E} \sim 0.0633$ N m^{-1},[83] $\theta \sim 128°$, the above relation suggests the threshold electric displacement field strength $D_z \sim 0.026$ C m^{-2}. To explore the possibility of field-induced infiltration in our hydrophobic pore, we consider a window of simulated electric displacement fields from zero to ~ 0.03 C m^{-2}. Reductions of the necessary strength of the field are possible by increasing wall−wall separations. A 2- or even 3-fold increase of d could be kinetically viable; however, the concomitant increase of evaporation times renders these situations less suitable for MD simulation studies.

In the presence of water, the actual electric field $\mathbf{E}$ is well below $\mathbf{D}/\varepsilon_o$ due to dielectric screening. In an isotropic aqueous phase, $\mathbf{E} = \mathbf{D}/\varepsilon_o\varepsilon_r$, however, this relation is inaccurate in a nanoconfinement where both $E_z(z)$ and (tensorial) relative permittivity show complex dependences on the distance from

the confinement walls.[84,85] Following previous work,[22] we obtain the first order estimate for the actual electric field inside the pore from local orientational polarization of water molecules. The average cosine of the angle between water dipoles and the direction of the field, θ_z, has been shown to provide a good measure of the field strength inside a field-exposed confinement.[86] In a recent study, we have shown[22] how the *change* of $\langle \cos \theta_z \rangle$ can inform us about the local field in systems with preexisting interfacial polarization[50] observed even in the absence of an external field. The reader is referred to ref 22 for details about the method and the calibration of $\Delta \langle \cos \theta \rangle$ vs E_z for the present model[61] of water. Panels a and b in Figure 3 illustrate spontaneous orientation of water dipoles inside the nanopore between a pair of butylated graphane disks with radius $r_{out} = 17$ Å at (methyl−methyl) separation $h = 11$ Å at zero field (a) and at $D_z = 0.031$ C m^{-2}, the strongest displacement field we consider (b). Panel c illustrates the estimated profile of the total field strength normal to the confinement walls, $E_z(z)$. For the specified displacement field D_z, the field strength inside the aqueous slab ($|z| \leq \sim 4$ Å) is shown to vary in the range of $\sim(1-2) \times 10^{-2}$ V Å^{-1}; hence, the total voltage across the slab is of $O(10^{-1})$ V. The mean of the inverse normal component of the relative permittivity inside the confined aqueous slab, $\langle \varepsilon_{zz}^{-1} \rangle$, is therefore between 20^{-1} and 30^{-1}. Fields of comparable strength can be routinely generated next to an AFM tip.[87] Using appropriate electrode insulation, μm aqueous films inside a capacitor at stationary field $E \sim 0.013$ V Å^{-1} have been found to be stable over arbitrarily long times of observation.[88] $O(10^{-2})$ V Å^{-1} fields barely exceed the linear regime of orientational polarization.[22,89] On the basis of the experimental polarizability of a water molecule, $\alpha \sim 1.5$ Å^3, these fields are too weak to induce a noticeable (>0.25%) change of molecular dipole in the liquid phase, and definitively well below the decomposition threshold field of $\sim$0.3 V Å^{-1}.[90,91]

III. RESULTS AND DISCUSSION

A. Abrupt Imposition, or Cessation of External Field.
For selected nanopore dimensions and ambient conditions ($P \sim 0$, $T = 300$ K), equilibration results in empty confinement regardless of initial configuration. The left panel of Figure 4 illustrates the uptake of water that follows the imposition of displacement field of strength 0.031 C m^{-2} (field corresponding to a capacitor electrode charge density of approximately an
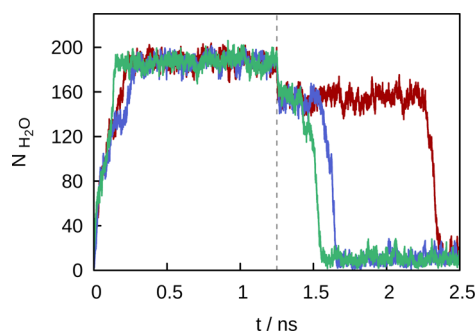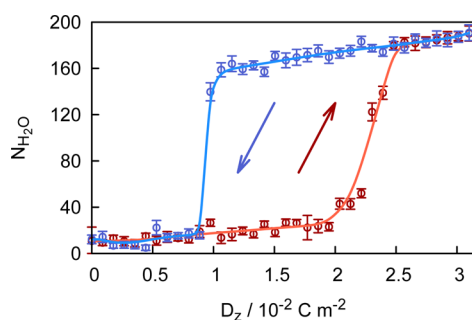
elementary charge per 6−7 nm^2). The initial, evacuated state is equilibrated in the absence of the field. While much of the pore in this state is empty, the number of confined (axial distance $r < r_{out}$) molecules, N_{H_2O}, fluctuates around 5−7% of the number observed in a fully wetted pore, an effect attributed to the convex shape of the liquid/vapor interface at the pore boundary.

The process of infiltration begins the moment the field is turned on and, for a given geometry, completes in $\sim$0.2 $\pm$ 0.05 ns. The rate of infiltration appears faster in the initial stage that corresponds to the adjustment in the meniscus curvature at the liquid/vapor interface in response to the attraction of water into the region under the field. The plots for three independent runs, illustrated in Figure 4, indicate about 25% of the pore volume is filled at this stage. The process proceeds at a somewhat slower pace, as further infiltration involves unfavorable wetting of pore walls. The final stage corresponds to the collapse of the vapor bubble in the center of the pore.

When the field is turned off (time $t = 1.25$ ns in Figure 4), we observe an immediate 17−19% decrease in water density inside the pore. The magnitude of this change is compatible with the reversal of electrostriction of the confined liquid phase, consistently observed upon imposition of similar fields in preceding works.[16,18,22,43] Once electrostriction is lost, water density fluctuates around the density of metastable liquid until a sufficient thermal fluctuation brings the system across the free energy barrier to cavitation. As the evaporation process depends on rare fluctuation events, the times of evaporation observed in multiple infiltration/expulsion cycles are scattered over a broad range from below 0.4 to several ns. Only about 0.1 ns elapses from the time of $\sim$15% depletion and complete evacuation. In many runs beginning in a fully wetted state and with the field turned off, not a single system has recovered its initial density after >15% depletion, suggesting the radius of the critical vapor nucleus R^* is around 6−7 Å. A mean field approximation for the barrier to vapor nucleation can be obtained by considering the surface free energy of a cylindrical bubble[25,31] of radius r, $\Delta\Omega(r) \sim 2\pi r d\gamma + 2\pi r^2 \gamma \cos \theta_c + P\pi r^2 d$, with the maximum at $r = r^* \sim 5.7$ Å. The estimated nucleus radius is in reasonable agreement with the apparent size of 6−7 Å deduced from the simulation. The mean field estimate for the barrier itself, $\Delta\Omega^*(r^*) \sim 7.9 \times 10^{-19}$ J or $\sim$19 k_BT is less reliable, exceeding more accurate umbrella sampling results for similar systems.[29−31,33] Applying umbrella sampling Monte Carlo, we determined[31] the evaporation barrier in a laterally extended pore of width $h = 14$ Å, $d \sim 10$ Å, and $\theta_c = 135°$ at 18.7 $\pm$ 1 k_BT. According to the known scaling relation $\Delta\Omega^* \propto d^2/\cos\theta_c$,[25,32] extrapolation to $d = 7$ Å and $\theta_c = 128°$ obtains $\Delta\Omega^* \sim 10.4$ k_BT, a value in reasonable agreement with observed evaporation kinetics. Using the observed evaporation times τ_e of $O(0.1-10)$ ns and the crude relation $\tau_e \sim (2\pi\hbar/k_BT) \exp(\Delta\Omega^*/k_BT)$ suggests activation barriers between 7 and 11 k_BT (k_B and $2\pi\hbar$ denote Boltzmann and Planck constants).

B. Uniformly Varying Field.
Response times observed in the above example suggest $O(10^{-1})$ GHz is the limiting field frequency the system would be able to follow.

To explore the temporal response further, and to identify the threshold field amplitude for pore wetting, we monitored the infiltration and expulsion processes under uniformly increasing or decreasing displacement fields. We compare the results for two rates of field change, $dD_z/dt = \pm 9 \times 10^{-3}$ C m^{-2} ns^{-1} or $\pm 4.5 \times 10^{-3}$ C m^{-2} ns^{-1}. Figure 5 describes a typical cycle in

Figure 4. Time dependence of the number of water molecules, N_{H_2O}, inside a nanopore with radius $r_{out} = 17$ Å, $r_{in} = 13$ Å, and $h = 11$ Å. The time origin corresponds to the imposition of the field ($D_z = 0.031$ C m^{-2}). The field is switched off at $t = 1.25$ ns. Different colors describe three independent runs under identical conditions.
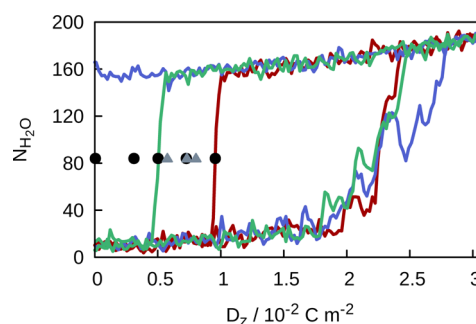
Figure 5. Typical density evolution, measured in terms of the number of water molecules, N_{H_2O}, inside a nanopore with radius r_{out} = 17 Å, r_{in} = 13 Å, and h = 11 Å, as a function of monotonically increasing (red curve) or decreasing (blue curve) electric displacement field D_z. The rate of field change, $dD_z/dt = \pm 9 \times 10^{-3}$ C m^{-2} s^{-1}.

Figure 6. A survey of 11 infiltration−expulsion cycles in neat water, described in terms of the number of water molecules, N_{H_2O}, in the nanopore (r_{out} = 17 Å, r_{in} = 13 Å, and h = 11 Å) as a function of electric displacement field D_z. Three cycles (red, blue, and green) are shown in full. As the shape of the cycles is similar in all cases, for the remaining eight cycles, we merely mark the positions of abrupt expulsion. Red, blue, and green curves and solid black circles correspond to the rate of field change dD_z/dt of $\pm 9 \times 10^{-3}$ C m^{-2} s^{-1}. The three gray triangles were obtained at a slower field decrease rate of -4.5×10^{-3} C m^{-2} s^{-1}. Infiltration branches determined at the slower field increase showed no appreciable difference from those obtained at a twice higher rate. One of the expulsion branches (blue) was completed at the time outside the plotted range.

terms of the dependence of the number of confined water molecules, N_{H_2O}, as a function of D_z for the bigger rate of $\pm 9 \times 10^{-3}$ C m^{-2} ns^{-1}. The weak initial response at fields below ∼2 $\times 10^{-2}$ C m^{-2} can be attributed to the change in the meniscus curvature discussed with Figure 4, while the rapid increase in N_{H_2O} in the range $(2.2-2.5) \times 10^{-2}$ C m^{-2} reflects full scale infiltration, which entails wetting of confinement walls. The threshold displacement field is surprisingly close to the continuum estimate of ∼2.5×10^{-2} C m^{-2} provided by eq 5. The gradual density rise beyond the infiltration transition is consistent with intensified electrostriction in a fully wetted nanopore.

The backward (expulsion) branch in the window of strong fields, where the pore is filled by the liquid, reflects the reduction in N_{H_2O} due to a gradual reversal of electrostriction with weakening of the field. In this regime, the backward branch coincides with the forward one. When the field is decreased below the threshold strength for infiltration, however, the liquid typically persists in the pore. The expulsion is delayed until the field strength falls much lower, generally below 10^{-2} C m^{-2}. In a fraction of runs, the field actually vanished before the evaporation took place. The pronounced hysteresis is explained by the activation barrier to expulsion, associated with the creation of the interface between the liquid and vapor phases. Conversely, the infiltration process begins with the liquid/vapor interface already in place and the area of the interface decreases as the pore is filled with water. The barrier to expulsion is expected to further increase in the presence of applied field, as the field stabilizes fully wetted states in comparison to the partially evacuated ones. We confirm this in trial calculations where we switch from the forward to backward branch before complete infiltration.

We survey a set of cycles where the field change was reversed after *complete* filling of the pores. Figure 6 summarizes the results of five cycles at the field change rate $dD_z/dt = \pm 9 \times 10^{-3}$ C m^{-2} ns^{-1}, along with an additional three cycles at a twice smaller rate of $\pm 4.5 \times 10^{-3}$ C m^{-2} ns^{-1}. The three cycles shown in different colors correspond to the higher rate. In one of them, evaporation took place after the field fell to zero. Regardless of the rate of field decay, evaporation was never observed at a displacement field above 0.01 C m^{-2}, which is below one-half of the threshold for infiltration. Wide scatter of evaporation events below this field reflects the rare event character of the process, rather than its reliance on further weakening of the field. The infiltration branches are more

reproducible. All of the remaining six cycles fell within the range of the three infiltration curves shown in Figure 6. Three of these six cycles were performed at twice slower field change, $dD_z/dt = \pm 4.5 \times 10^{-3}$ C m^{-2} ns^{-1}, yet we observe no systematic deviation from the results obtained at the higher rate. The only significant difference between individual cycles was found in times, and associated field strengths, corresponding to abrupt evaporation events. We identify these events by registering positions of 50% evacuation. In Figure 6, they are marked by solid circles (higher field change rate) or triangles (slower rate). Interestingly, all evaporation events observed at the slower rate are grouped within the displacement field interval of $D_z = (0.5-1.0) \times 10^{-2}$ C m^{-2}. Poor reproducibility of the backward (evacuation) branch confirms these are rare events. By and large, evaporation times of 10 ns suffice for complete evacuation of water from the nanopore even when the field is turned off smoothly rather than in a stepwise fashion.

C. Electrolyte Solution. So far, we have considered only pure water. Dissolved ions could, however, be present in many applications, ranging from nanofluidics to controlled permeation of porous electrode materials. In addition to electrostatic shielding, ions can modulate field effects on nanopore wetting by supporting electro-osmotic flow in the channels.[14] These possibilities are examined by extending our model calculations to cases where pure water is replaced by NaCl solutions. We used a relatively high bulk molality of 1.027 mol kg^{-1} to amplify any changes. Salt concentration in a hydrophobic confinement is lower than in the surrounding bath, due to reduced opportunities for ion hydration and low permittivity of the walls.[53] Statistics in molality calculations for the 7 Å wide confinement is poor. In Figure 7 we illustrate the qualitative trend by comparing confined and bulk NaCl molalities in bigger pores. They are made up of identical wall material but with diameter 64 Å, r_{out} = 32 Å and d = 15 Å. We use three values of r_{in}, 24, 16, or 8 Å and the displacement field D_z = 0.031 C m^{-2}. Despite attraction by the field, the interior ion concentration remains at about 70 ± 5% of the bulk one. For
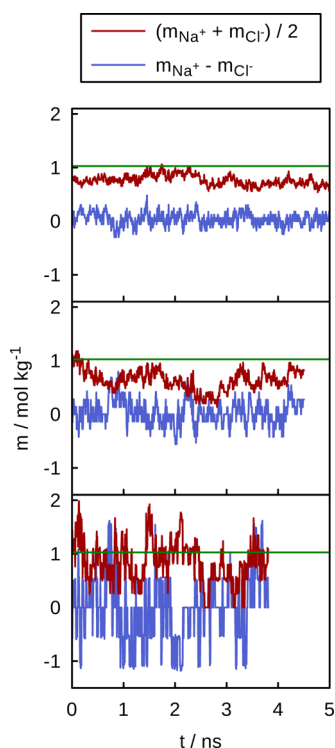
Figure 7. Time dependence of ion molalities: $(m_{Na+} + m_{Cl-})/2$ (red) and $(m_{Na+} - m_{Cl-})$ (blue) as a measure of deviation from neutrality inside the confinement core ($r \leq r_{in}$ with wall separation $h = 19$ Å and radius $r_{out} = 32$ Å). The field corresponds to $D_z = 0.031$ C m^{-2}. $r_{in} = 24$ Å (top), 16 Å (middle), or 8 Å (bottom graph). The average electrolyte concentration in the confinement core is around 30% below the bulk value of 1.027 mol kg^{-1} (green line).

the smallest core volume, $r_{in} = 8$ Å, only a handful of ions are present and we observe frequent deviations from local neutrality with a slight preference for Cl− ions. The trend toward salt depletion intensifies in the narrow slit with $d = 7$ Å. Here, ions with an intact first hydration shell are limited to a thin layer of $|z| \leq 1$ Å from the midplane of the pore. The remaining core molality of the ions shows big fluctuations around the average value of $O(0.1)$ mol kg^{-1} with strong dominance of sodium ions. A small number of confined ions (0 to $O(1)$) precludes accurate statistics of ion molalities in these pores.

Figure 8 illustrates several filling/emptying cycles analogous to those shown in Figure 6, except that the liquid was 1.027 mol kg^{-1} NaCl solution. The rate of field change is $dD_z/dt = \pm 9 \times 10^{-3}$ C m^{-2} ns^{-1}. While not explicitly measured, any contribution of electro-osmotic flow is implicitly captured in the simulation in the presence of salt ions. Within the noise associated with thermal fluctuations, the curves obtained in the presence of the salt are hardly distinguishable from those shown in Figures 5 and 6 for pure water. Likewise, the simulated infiltration under the slowly changing field, $dD_z/dt = \pm 4.5 \times 10^{-3}$ C m^{-2} ns^{-1} (Figure 9), reveals no change compared to the faster process shown in Figure 8. The small increase in saline contact angle, compared to that of pure water,[58] shifts the infiltration transition to a stronger displacement field. This change is consistent with a salt-induced increase of infiltration pressure observed[8] in wider nanopores. While the addition of salt has shown a moderate hysteresis reduction of the infiltration−expulsion cycle under pressure control,[7,8] no
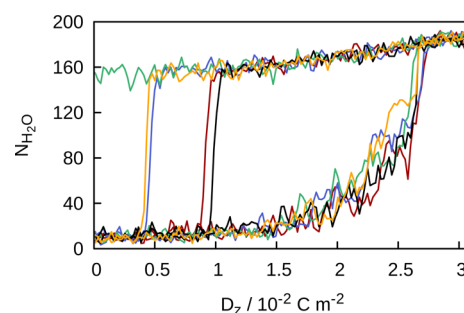
Figure 8. Infiltration (lower) and expulsion (upper) branches in 1.027 mol kg^{-1} NaCl solution, described by plotting the number of water molecules, N_{H_2O}, inside a nanopore with radius $r_{out} = 17$ Å, $r_{in} = 13$ Å, and $h = 11$ Å, in five independent cycles under identical conditions. The rate of field increase and subsequent decrease dD_z/dt was $\pm 9 \times 10^{-3}$ C m^{-2} s^{-1}.
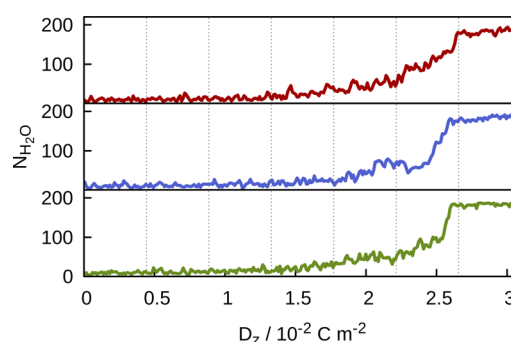

Figure 9. Infiltration branches in 1.027 mol kg^{-1} NaCl showing the number of water molecules, N_{H_2O}, inside a nanopore with radius $r_{out} = 17$ Å, $r_{in} = 13$ Å, and $h = 11$ Å, as a function of monotonically increasing electric displacement field D_z. The rate of field change (dD_z/dt) was 4.5×10^{-3} C m^{-2} s^{-1}. Different colors correspond to independent runs under identical conditions.

statistically meaningful trend could be deduced from our simulation results. Notwithstanding small quantitative adjustments, the above comparisons indicate our findings obtained in pure water simulations also apply to salt solutions, at least for selected conditions.

D. Incomplete Cycles. To estimate the position of the activation barrier to water expulsion in the presence of the field, in a number of runs started under uniformly increasing D_z, we initiate the reverse process (field decrease) from incompletely filled configurations. As illustrated by the examples presented in Figure 10, if the infiltration already reached ∼65−70% completion, it promptly proceeded toward the fully filled state even under *decreasing* field. This result indicates the likely radius of the critical vapor nucleus, $r^*(D_z)$, corresponding to the activation barrier for evaporation at the specified field strength ($D_z \sim 0.025$ C m^{-2}) to be around 8.5 ± 1 Å. This value is comparable to the mean field prediction. In analogy with our earlier estimate of the nucleus size in the absence of the field (section A), one can approximate free energy of cavitation as a function of the radius of cylindrical vapor cavity in the pore center for finite D_z[16]

$$\Delta\Omega(r, D_z) \sim 2\pi r d\gamma + 2\pi r^2 \gamma \cos\theta_c + \left[P + \frac{D_z^2}{2\varepsilon_o}\left(1 - \frac{1}{\varepsilon_r}\right)\right]\pi r^2 d$$

(7)
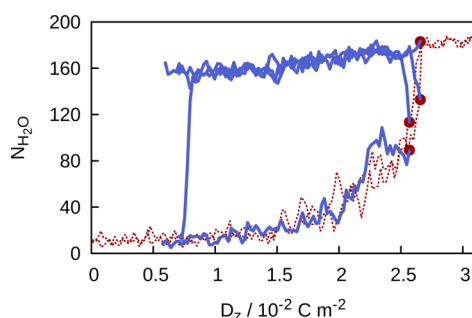
Figure 10. Density evolution (quantified in terms of the number of water molecules, N_{H_2O}) in four backward runs (decreasing field, $dD_z/dt = -9 \times 10^{-3}$ C m^{-2} s^{-1}) inside a nanopore with radius $r_{out} = 17$ Å, $r_{in} = 13$ Å, and $h = 11$ Å. The runs were initiated at four configurations (solid circles) taken from previous infiltration (increasing field) branches (dashed red). The data are indicative of a shallow barrier to infiltration at about 50% filling.

At $D_z \sim 0.025$ C m^{-2}, $\Delta\Omega(r, D_z)$ passes through the maximum at $r^* \sim 8.3$ Å. If the field begins decreasing *before* the vapor cavity shrinks below the critical size r^*, infiltration is reversed without delay. However, once the cavity collapses, because of Maxwell stress contribution (the last term in eq 7), the barrier to vapor nucleation remains prohibitive (upper-bound mean field estimate $\Delta\Omega(r^*, D_z) \sim 27\ k_BT$), delaying eventual expulsion until D_z is significantly reduced. In our simulations, expulsion occurred only at displacement fields below ~ 0.01 C m^{-2}. The same applied to 1 mol kg^{-1} NaCl solution, and we observe no significant effect of added salt on the hysteresis of the filling/emptying cycle.

While we focused on a single pore size because of computational constraints, extrapolations to other sizes are possible on the basis of our results and fair agreement with mean field relations, eqs 1, 5, and 6. According to eq 5, increasing the pore diameter d will reduce the magnitude of displacement field required for infiltration. Because of the steep rise of the activation barrier[29,32] to expulsion with d, in the case of water, the increase in d is limited to below 10 molecular diameters.[25,26,30,31,33] Combining the effect of the field *and* external pressure, on the other hand, can facilitate intrusion when the pores prove too narrow to be wetted under electric field alone.[12] On the basis of eq 6, electric control of nanopore filling can be extended to other nonwetting liquids provided the inverse dielectric constant, ε_r^{-1}, is sufficiently different from unity, a condition fulfilled by strongly *and* moderately polar liquids.

IV. CONCLUDING REMARKS

Our molecular simulations show an applied electric field can enable *reversible* control of wetting and dewetting in hydrophobic nanochannels. In similar experimental and theoretical studies, reversal of filling transition relied on the remnants of air or vapor inside the wetted pores. In narrow carbon nanotube pores conducive to spontaneous expulsion, on the other hand, infiltration required increased pressure in addition to the field.[12] Using appropriate pore geometry, we observe complete wetting/drying transitions inside the confinement, controlled solely by the applied field.

Fair estimates of critical pore dimensions and required external field, as well as the dimensions of the vapor nuclei associated with the kinetic barrier to water expulsion, can be obtained from a continuum/mean field picture. Neglecting

crucial thermal fluctuations, this approach is adequate to predict qualitative trends but overestimates absolute magnitudes of activation barriers.[29] In ~ 1 nm sized pores, kinetic barriers result in pronounced wetting−dewetting hysteresis, yet they cannot support long-lived metastable confined liquid phases unless assisted by at least a fraction of the field initially required for infiltration. Our observations in neat water remain essentially unchanged in the presence of salt ions. The addition of salt slightly increases the threshold field for infiltration but does not appear to alleviate the hysteresis, as indicated in earlier measurements.[8] Our studies set the stage for the design of field-controlled nanofluidic valves, regulated pore permeation, absorption of surface energy in a hydrophobic porous medium, and nanofluidic transistors[92] driven by electrically stimulated phase transitions.

■ AUTHOR INFORMATION

Corresponding Authors
*E-mail: dbratko@vcu.edu.
*E-mail: aluzar@vcu.edu.
Notes
The authors declare no competing financial interest.

■ ACKNOWLEDGMENTS

■ REFERENCES

(1) Powell, M. R.; Cleary, L.; Davenport, M.; Shea, K. J.; Siwy, Z. S. Electric-field-induced wetting and dewetting in single hydrophobic nanopores. *Nat. Nanotechnol.* **2011**, *6* (12), 798−802.

(2) Smirnov, S. N.; Vlassiouk, I. V.; Lavrik, N. V. Voltage-Gated Hydrophobic Nanopores. *ACS Nano* **2011**, *5* (9), 7453−7461.

(3) Lifton, V. A.; Taylor, J. A.; Vyas, B.; Kolodner, P.; Cirelli, R.; Basavanhally, N.; Papazian, A.; Frahm, R.; Simon, S.; Krupenkin, T. Superhydrophobic membranes with electrically controllable permeability and their application to "smart" microbatteries. *Appl. Phys. Lett.* **2008**, *93* (4), 043112.

(4) Eroshenko, V.; Regis, R. C.; Soulard, M.; Patarin, J. Energetics: A new field of applications for hydrophobic zeolites. *J. Am. Chem. Soc.* **2001**, *123* (33), 8129−8130.

(5) Eroshenko, V.; Regis, R. C.; Soulard, M.; Patarin, J. The heterogeneous systems 'water-hydrophobic zeolites': new molecular springs. *C. R. Phys.* **2002**, *3* (1), 111−119.

(6) Soulard, M.; Patarin, J.; Eroshenko, V.; Regis, R. Molecular spring or bumper: A new application for hydrophobic zeolitic materials. In *Recent Advances in the Science and Technology of Zeolites and Related Materials, Pts. A-C*; 2004; Vol. 154, pp 1830−1837.

(7) Kong, X. G.; Surani, F. B.; Qiao, Y. Energy absorption of nanoporous silica particles in aqueous solutions of sodium chloride. *Phys. Scr.* **2006**, *74* (5), 531−534.

(8) Kong, X.; Qiao, Y. Improvement of recoverability of a nanoporous energy absorption system by using chemical admixture. *Appl. Phys. Lett.* **2005**, *86* (15), 151919.

(9) Krupenkin, T.; Taylor, J. A.; Kolodner, P.; Hodes, M. Electrically tunable superhydrophobic nanostructured surfaces. *Bell Labs Tech. J.* **2005**, *10* (3), 161−170.

(10) Krupenkin, T. N.; Taylor, J. A.; Wang, E. N.; Kolodner, P.; Hodes, M.; Salamon, T. R. Reversible wetting-dewetting transitions on electrically tunable superhydrophobic nanostructured surfaces. *Langmuir* **2007**, *23* (18), 9128–9133.

(11) Smirnov, S.; Vlassiouk, I.; Takmakov, P.; Rios, F. Water Confinement in Hydrophobic Nanopores. Pressure-Induced Wetting and Drying. *ACS Nano* **2010**, *4* (9), 5069–5075.

(12) Xu, B. X.; Qiao, Y.; Zhou, Q. L.; Chen, X. Effect of Electric Field on Liquid Infiltration into Hydrophobic Nanopores. *Langmuir* **2011**, *27* (10), 6349–6357.

(13) Vaitheeswaran, S.; Rasaiah, J. C.; Hummer, G. Electric field and temperature effects on water in the narrow nonpolar pores of carbon nanotubes. *J. Chem. Phys.* **2004**, *121* (16), 7955–7965.

(14) Takhistov, P.; Indeikina, A.; Chang, H. C. Electrokinetic displacement of air bubbles in microchannels. *Phys. Fluids* **2002**, *14* (1), 1–14.

(15) Liu, J.; Wang, M. R.; Chen, S.; Robbins, M. O. Uncovering Molecular Mechanisms of Electrowetting and Saturation with Simulations. *Phys. Rev. Lett.* **2012**, *108* (21), 216101.

(16) Dzubiella, J.; Hansen, J. P. Electric-field-controlled water and ion permeation of a hydrophobic nanopore. *J. Chem. Phys.* **2005**, *122* (23), 234706.

(17) Vaitheeswaran, S.; Yin, H.; Rasaiah, J. C. Water between plates in the presence of an electric field in an open system. *J. Phys. Chem. B* **2005**, *109* (14), 6629–6635.

(18) Bratko, D.; Daub, C. D.; Leung, K.; Luzar, A. Effect of field direction on electrowetting in a nanopore. *J. Am. Chem. Soc.* **2007**, *129* (9), 2504–2510.

(19) Sacha, G. M.; Verdaguer, A.; Salmeron, M. Induced water condensation and bridge formation by electric fields in atomic force microscopy. *J. Phys. Chem. B* **2006**, *110* (30), 14870–14873.

(20) Lu, W.; Kim, T.; Han, A.; Qiao, Y. Electrically controlling infiltration pressure in nanopores of a hexagonal mesoporous silica. *Mater. Chem. Phys.* **2012**, *133* (1), 259–262.

(21) Daub, C. D.; Bratko, D.; Luzar, A. Nanoscale Wetting Under Electric Field from Molecular Simulations. *Top. Curr. Chem.* **2012**, *307*, 155–180.

(22) Vanzo, D.; Bratko, D.; Luzar, A. Nanoconfined water under electric field at constant chemical potential undergoes electrostriction. *J. Chem. Phys.* **2014**, *140*, 074710.

(23) Gomez-Monivas, S.; Saenz, J. J.; Calleja, M.; Garcia, R. Field-induced formation of nanometer-sized water bridges. *Phys. Rev. Lett.* **2003**, *91* (5), 056101.

(24) Gupta, R.; Olivier, G. K.; Frechette, J. Invariance of the Solid-Liquid Interfacial Energy in Electrowetting Probed via Capillary Condensation. *Langmuir* **2010**, *26* (14), 11946–11950.

(25) Yaminsky, V. V.; Yushchenko, V. S.; Amelina, E. A.; Shchukin, E. D. Cavity Formation Due to a Contact between Particles in a Nonwetting Liquid. *J. Colloid Interface Sci.* **1983**, *96* (2), 301–306.

(26) Lum, K.; Luzar, A. Pathway to surface-induced phase transition of a confined fluid. *Phys. Rev. E* **1997**, *56* (6), R6283–R6286.

(27) Lum, K.; Chandler, D. Phase diagram and free energies of vapor films and tubes for a confined fluid. *Int. J. Thermophys.* **1998**, *19* (3), 845–855.

(28) Lum, K.; Chandler, D.; Weeks, J. D. Hydrophobicity at small and large length scales. *J. Phys. Chem. B* **1999**, *103* (22), 4570–4577.

(29) Leung, K.; Luzar, A. Dynamics of capillary evaporation. II. Free energy barriers. *J. Chem. Phys.* **2000**, *113* (14), 5845–5852.

(30) Bratko, D.; Curtis, R. A.; Blanch, H. W.; Prausnitz, J. M. Interaction between hydrophobic surfaces with metastable intervening liquid. *J. Chem. Phys.* **2001**, *115* (8), 3873–3877.

(31) Leung, K.; Luzar, A.; Bratko, D. Dynamics of capillary drying in water. *Phys. Rev. Lett.* **2003**, *90*, 065502.

(32) Luzar, A. Activation barrier scaling for the spontaneous evaporation of confined water. *J. Phys. Chem. B* **2004**, *108* (51), 19859–19866.

(33) Sharma, S.; Debenedetti, P. G. Free Energy Barriers to Evaporation of Water in Hydrophobic Confinement. *J. Phys. Chem. B* **2012**, *116* (44), 13282–13289.

(34) Evans, R. Fluids Adsorbed in Narrow Pores - Phase-Equilibria and Structure. *J. Phys.: Condens. Matter* **1990**, *2* (46), 8989–9007.

(35) Frank, H. S. *J. Chem. Phys.* **1955**, *23*, 2023.

(36) Luzar, A.; Bratko, D.; Blum, L. Monte-Carlo Simulation of Hydrophobic Interaction. *J. Chem. Phys.* **1987**, *86* (5), 2955–2959.

(37) Wallqvist, A.; Berne, B. J. Computer-Simulation Of Hydrophobic Hydration Forces On Stacked Plates At Short-Range. *J. Phys. Chem.* **1995**, *99* (9), 2893–2899.

(38) Truskett, T. M.; Debenedetti, P. G.; Torquato, S. Thermodynamic implications of confinement for a waterlike fluid. *J. Chem. Phys.* **2001**, *114* (5), 2401–2418.

(39) Chandler, D. Interfaces and the driving force of hydrophobic assembly. *Nature* **2005**, *437*, 640–647.

(40) Giovambattista, N.; Rossky, P. J.; Debenedetti, P. G. Effect of pressure on the phase behavior and structure of water confined between nanoscale hydrophobic and hydrophilic plates. *Phys. Rev. E* **2006**, *73* (4), 041604.

(41) Rasaiah, J. C.; Garde, S.; Hummer, G. Water in nonpolar confinement: From nanotubes to proteins and beyond. *Annu. Rev. Phys. Chem.* **2008**, *59*, 713–740.

(42) England, J. L.; Park, S.; Pande, V. S. Theory for an order-driven disruption of the liquid state in water. *J. Chem. Phys.* **2008**, *128* (4), 044503.

(43) Bratko, D.; Daub, C. D.; Luzar, A. Field-exposed water in a nanopore: liquid or vapour? *Phys. Chem. Chem. Phys.* **2008**, *10* (45), 6807–6813.

(44) Bratko, D.; Daub, C. D.; Luzar, A. Water-mediated ordering of nanoparticles in an electric field. *Faraday Discuss.* **2009**, *141*, 55–66.

(45) Lee, C. Y.; McCammon, J. A.; Rossky, P. J. The Structure Of Liquid Water At An Extended Hydrophobic Surface. *J. Chem. Phys.* **1984**, *80* (9), 4448–4455.

(46) Luzar, A.; Svetina, S.; Zeks, B. Consideration of The Spontaneous Polarization of Water at the Solid Liquid Interface. *J. Chem. Phys.* **1985**, *82* (11), 5146–5154.

(47) Lee, S. H.; Rossky, P. J. A Comparison of the Structure and Dynamics of Liquid Water at Hydrophobic and Hydrophilic Surfaces - A Molecular-Dynamics Simulation Study. *J. Chem. Phys.* **1994**, *100* (4), 3334–3345.

(48) Daub, C. D.; Bratko, D.; Leung, K.; Luzar, A. Electrowetting at the nanoscale. *J. Phys. Chem. C* **2007**, *111* (2), 505–509.

(49) Daub, C. D.; Bratko, D.; Ali, T.; Luzar, A. Microscopic Dynamics of the Orientation of a Hydrated Nanoparticle in an Electric Field. *Phys. Rev. Lett.* **2009**, *103*, 207801.

(50) von Domaros, M.; Bratko, D.; Kirchner, B.; Luzar, A. Dynamics at a Janus Interface. *J. Phys. Chem. C* **2013**, *117* (9), 4561–4567.

(51) Bier, M.; Ibagon, I. Density functional theory of electrowetting. *Phys. Rev. E* **2014**, *89* (4), 042409.

(52) Yeo, L. Y.; Chang, H. C. Electrowetting films on parallel line electrodes. *Phys. Rev. E* **2006**, *73* (1), 011605.

(53) Bratko, D.; Jonsson, B.; Wennerstrom, H. Electrical Double-Layer Interactions with Image Charges. *Chem. Phys. Lett.* **1986**, *128* (5–6), 449–454.

(54) Frenkel, D.; Smit, B. *Understanding molecular simulation, from algorithms to applications*; Academic: San Diego, CA, 2002.

(55) Bolhuis, P. G.; Chandler, D. Transition path sampling of cavitation between molecular scale solvophobic surfaces. *J. Chem. Phys.* **2000**, *113* (8), 8154–8160.

(56) Lei, Y. J.; Leng, Y. S. Hydrophobic Drying and Hysteresis at Different Length Scales by Molecular Dynamics Simulations. *Langmuir* **2012**, *28* (6), 3152–3158.

(57) Choudhury, N.; Pettitt, B. M. On the mechanism of hydrophobic association of nanoscopic solutes. *J. Am. Chem. Soc.* **2005**, *127* (10), 3556–3567.

(58) Daub, C. D.; Bratko, D.; Luzar, A. Electric Control of Wetting by Salty Nanodrops: Molecular Dynamics Simulations. *J. Phys. Chem. C* **2011**, *115* (45), 22393–22399.

(59) Kalluri, R. K.; Biener, M. M.; Suss, M. E.; Merrill, M. D.; Stadermann, M.; Santiago, J. G.; Baumann, T. F.; Biener, J.; Striolo, A. Unraveling the potential and pore-size dependent capacitance of slit-

shaped graphitic carbon pores in aqueous electrolytes. *Phys. Chem. Chem. Phys.* **2012**, *15* (7), 2309−2320.

(60) Kalluri, R. K.; Konatham, D.; Striolo, A. Aqueous NaCl Solutions within Charged Carbon-Slit Pores: Partition Coefficients and Density Distributions from Molecular Dynamics Simulations. *J. Phys. Chem. C* **2011**, *115* (28), 13786−13795.

(61) Berendsen, H. J. C.; Grigera, J. R.; Straatsma, T. P. The Missing Term In Effective Pair Potentials. *J. Phys. Chem.* **1987**, *91* (24), 6269−6271.

(62) Vega, C.; Abascal, J. L. F.; Conde, M. M.; Aragones, J. L. What ice can teach us about water interactions: a critical comparison of the performance of different water models. *Faraday Discuss.* **2009**, *141*, 251−276.

(63) Bako, I.; Ricci, M. A.; Debenedetti, P. G.; Rovere, M.; Havenith, M.; Coudert, F. X.; Luzar, A.; Klein, J.; Jungwirth, P.; Yamaguchi, T.; et al. Discussion. *Faraday Discuss.* **2009**, *141*, 443−465.

(64) Milischuk, A. A.; Ladanyi, B. M. Structure and dynamics of water confined in silica nanopores. *J. Chem. Phys.* **2011**, *35*, 174709.

(65) Aragones, J. L.; MacDowell, L. G.; Siepmann, J. I.; Vega, C. Phase Diagram of Water under an Applied Electric Field. *Phys. Rev. Lett.* **2011**, *107* (15), 155702.

(66) Gereben, O.; Pusztai, L. On the accurate calculation of the dielectric constant from molecular dynamics simulations: The case of SPC/E and SWM4-DP water. *Chem. Phys. Lett.* **2008**, *507* (1−3), 80−83.

(67) Agarwal, M.; Alam, M. P.; Chakravarty, C. Thermodynamic, Diffusional, and Structural Anomalies in Rigid-Body Water Models. *J. Phys. Chem. B* **2011**, *115* (21), 6935−6945.

(68) Cheng, L. J.; Chang, H. C. Microscale pH regulation by splitting water. *Biomicrofluidics* **2011**, *5* (4), 046502.

(69) Vanzo, D.; Bratko, D.; Luzar, A. Wettability of pristine and alkyl-functionalized graphane. *J. Chem. Phys.* **2012**, *137* (3), 034707.

(70) Sofo, J. O.; Chaudhari, A. S.; Barber, G. D. Graphane: A two-dimensional hydrocarbon. *Phys. Rev. B* **2007**, *75* (15), 153401.

(71) Elias, D. C.; Nair, R. R.; Mohiuddin, T. M. G.; Morozov, S. V.; Blake, P.; Halsall, M. P.; Ferrari, A. C.; Boukhvalov, D. W.; Katsnelson, M. I.; Geim, A. K.; Novoselov, K. S. Control of Graphene's Properties by Reversible Hydrogenation: Evidence for Graphane. *Science* **2009**, *323* (5914), 610−613.

(72) Lebegue, S.; Klintenberg, M.; Eriksson, O.; Katsnelson, M. I. Accurate electronic band gap of pure and functionalized graphane from GW calculations. *Phys. Rev. B* **2009**, *79* (24), 245117.

(73) Tavares, F. W.; Bratko, D.; Blanch, H. W.; Prausnitz, J. M. Ion-Specific Effects in the Colloid-Colloid or Protein-Protein Potential of Mean Force: Role of Salt-Macroion van der Waals Interactions. *J. Phys. Chem. B* **2004**, *108* (26), 9228−9235.

(74) Vanzo, D.; Bratko, D.; Luzar, A. Tunable Wetting of Surfaces with Ionic Functionalities. *J. Phys. Chem. C* **2012**, *116* (29), 15467−15473.

(75) Fyta, M.; Netz, R. R. Ionic force field optimization based on single-ion and ion-pair solvation properties: Going beyond standard mixing rules. *J. Chem. Phys.* **2012**, *136* (12), 124103.

(76) Yeh, I. C.; Berkowitz, M. L. Ewald summation for systems with slab geometry. *J. Chem. Phys.* **1999**, *111* (7), 3155−3162.

(77) Raj, R.; Maroo, S. C.; Wang, E. N. Wettability of Graphene. *Nano Lett.* **2013**, *13* (4), 1509−1515.

(78) Shih, C. J.; Strano, M. S.; Blankschtein, D. Wetting translucency of graphene. *Nat. Mater.* **2013**, *12* (10), 866−869.

(79) Driskill, J.; Vanzo, D.; Bratko, D.; Luzar, A. Wetting transparency of graphene on water. *J. Chem. Phys.* **2014**, *141*, 18C517.

(80) Mugele, F.; Baret, J. C. Electrowetting: From basics to applications. *J. Phys.: Condens. Matter* **2005**, *17* (28), R705−R774.

(81) Shapiro, B.; Moon, H.; Garrell, R. L.; Kim, C. J. Equilibrium behavior of sessile drops under surface tension, applied external fields, and material variations. *J. Appl. Phys.* **2003**, *93* (9), 5794−5811.

(82) Dzubiella, J.; Hansen, J. P. Competition of hydrophobic and Coulombic interactions between nanosized solutes. *J. Chem. Phys.* **2004**, *121* (11), 5514−5530.

(83) Kolafa, J.; Viererblova, L. Static Dielectric Constant from Simulations Revisited: Fluctuations or External Field? *J. Chem. Theory Comput.* **2014**, *10* (4), 1468−1476.

(84) Ballenegger, V.; Hansen, J. P. Dielectric permittivity profiles of confined polar fluids. *J. Chem. Phys.* **2005**, *122* (11), 114711.

(85) Bonthuis, D. J.; Gekle, S.; Netz, R. R. Profile of the Static Permittivity Tensor of Water at Interfaces: Consequences for Capacitance, Hydration Interaction and Ion Adsorption. *Langmuir* **2012**, *28* (20), 7679−7694.

(86) Yeh, I. C.; Berkowitz, M. L. Dielectric constant of water at high electric fields: Molecular dynamics study. *J. Chem. Phys.* **1999**, *110* (16), 7935−7942.

(87) Philippsen, A.; Im, W. P.; Engel, A.; Schirmer, T.; Roux, B.; Muller, D. J. Imaging the electrostatic potential of transmembrane channels: Atomic probe microscopy of OmpF porin. *Biophys. J.* **2002**, *82* (3), 1667−1676.

(88) Song, C. R.; Wang, P. S. High electric field effects on gigahertz dielectric properties of water measured with microwave microfluidic devices. *Rev. Sci. Instrum.* **2010**, *81* (5), 054702.

(89) Sutmann, G. Structure formation and dynamics of water in strong external electric fields. *J. Electroanal. Chem.* **1998**, *450* (2), 289−302.

(90) Stuve, E. M. Ionization of water in interfacial electric fields: An electrochemical view. *Chem. Phys. Lett.* **2012**, *519*−20, 1−17.

(91) Saitta, M. A.; Saija, F.; Giaquinta, P. Ab initio molecular dynamics study of dissociation of water under an electric field. *Phys. Rev. Lett.* **2012**, 207801.

(92) Karnik, R.; Fan, R.; Yue, M.; Li, D. Y.; Yang, P. D.; Majumdar, A. Electrostatic control of ions and molecules in nanofluidic transistors. *Nano Lett.* **2005**, *5* (5), 943−948.

(93) Jorgensen, W. L.; Madura, J. D.; Swenson, C. J. Optimized Intermolecular Potential Functions for Liquid Hydrocarbons. *J. Am. Chem. Soc.* **1984**, *106* (22), 6638−6646.

■ NOTE ADDED AFTER ASAP PUBLICATION

This paper was published ASAP on October 15, 2014. Citation numbering was corrected. The corrected paper was reposted on October 23, 2014.